Nanoscale Advances

ROYAL SOCIETY OF CHEMISTRY

PAPER

View Article Online
View Journal | View Issue

Cite this: *Nanoscale Adv.*, 2025, **7**, 1742

Insights into the electronic structure, optical properties, and photocatalytic potential of Gd_2CoCrO_6 perovskite: a comprehensive theoretical and experimental investigation†

M. J. Hosen, ‡[ab] M. Tarek, ‡[b] M. D. I. Bhuyan, [bc] M. A. Basith *[b] and I. M. Syed[a]

In this study, we present a comprehensive theoretical and experimental investigation into the electronic structure, optical properties, and photocatalytic potential of Gd_2CoCrO_6 (GCCO) double perovskite. Using first-principles calculations with the generalized-gradient-approximation plus Hubbard *U* (GGA + *U*) method, we explored the effects of Coulomb interactions on the electronic properties. Our calculations revealed that GCCO exhibits a half-metallic nature, displaying metallic behavior for up-spin and semiconducting behavior for down-spin states. The optimized U_{eff} value of 4.2 eV accurately reproduces the direct bandgap of 2.25 eV, which aligns closely with experimental results obtained through UV-visible absorption spectroscopy and photoluminescence analysis. Additionally, time-resolved photoluminescence (TRPL) measurements indicate a mean charge carrier lifetime of 2.37 ns, suggesting effective charge separation. Mott–Schottky analysis and valence band X-ray photoelectron spectroscopy (XPS) confirm the n-type semiconducting nature of GCCO with favorable band edge positions for redox reactions. The combination of theoretical insights and experimental characterization indicates that GCCO holds significant promise as a photocatalyst for applications in renewable energy production and environmental remediation, particularly in solar-driven water splitting and pollutant degradation. Our study provides crucial insights into the electronic structure and optical properties of double perovskites like GCCO, highlighting their suitability for photocatalytic applications. Furthermore, the research paves the way for future work in the compositional engineering and defect modulation of double perovskites to optimize their photocatalytic efficiency.

Received 11th December 2024
Accepted 23rd January 2025

DOI: 10.1039/d4na01033g

rsc.li/nanoscale-advances

1. Introduction

Perovskite oxides have drawn significant attention over the last 70 years for their remarkable multifunctional characteristics and broad range of technical applications.[1–4] Notably, previous investigations have shown that double perovskites, represented by the formula $A_2BB'O_6$ (where A denotes rare-earth elements and B and B′ are transition metals), offer greater flexibility and a wider array of properties than simple perovskites as a result of the presence of two distinct transition metals at the B sites.[5–7] These perovskite materials display a spectrum of electronic behaviors, from metallic to insulating, even half-metallic, having spin-polarized orientation. Additionally, they exhibit magnetic ordering, multiferroic properties, superconductivity, and catalytic activity.[3,8–10] These properties enable their use across various fields, including spintronics, data storage, microelectronics, quantum electromagnets, and sensor technologies.[3,6,11] Furthermore, the semiconducting nature of double perovskites makes them suitable for photochemical energy storage, photovoltaics, and photocatalytic applications.[12–15] These excellent optical, magnetic, and electronic properties of $A_2BB'O_6$ double-perovskites, along with their promising applications, inspired us to explore the double perovskite Gd_2CoCrO_6.

However, synthesizing a fully organized structure of A_2CoCrO_6 double-perovskite is challenging owing to anti-site disorder, arising from the nearly equal ionic radii of Cr^{3+} and Co^{2+} ions (0.62 Å and 0.65 Å, respectively).[16,17] Due to difficulties in managing the order-disorder effect during the synthesis, the double perovskite family of A_2CoCrO_6 has not been explored yet. We have recently synthesized GCCO double-perovskite nanoparticles successfully by improving the synthesis step of the sol–gel process and explored their structure, surface morphology,

[a]*Department of Physics, University of Dhaka, Dhaka-1000, Bangladesh*

[b]*Nanotechnology Research Laboratory, Department of Physics, Bangladesh University of Engineering and Technology, Dhaka-1000, Bangladesh. E-mail: mabasith@phy.buet.ac.bd*

[c]*Department of Physics, Mawlana Bhashani Science and Technology University, Santosh 1902, Bangladesh*

† Electronic supplementary information (ESI) available. See DOI: https://doi.org/10.1039/d4na01033g

‡ These authors contributed equally.

magnetic, and optical features extensively for the first time.[17] Notably, the favorable bandgap and band edge position of the GCCO double perovskite unveils its excellent potential for photocatalytic O_2 and H_2 generation from water. Furthermore, the lack of the necessary experimental facilities makes it extremely difficult to conduct an experimental analysis of the material characteristics of double-perovskites at the atomic scale. However, by doing the first-principles computation based on density-functional theory (DFT), these constraints can be greatly eliminated.[18]

Moreover, standard DFT approximations, such as generalized-gradient-approximation (GGA) and local-density-approximation (LDA), are unable to describe accurately the strongly correlated systems like $A_2BB'O_6$ owing to the presence of transition metal 3d and rare earth 4f-orbitals.[19] Because of the strongly correlated 4f/3d orbitals, the GGA and LDA approaches show systematic difficulties in describing the onsite Coulomb repulsion.[20] Especially the GGA and LDA approaches show a significant discrepancy in estimating the optical bandgap, which is essential for explaining the optoelectronic and photocatalytic properties of a material.[21,22] To address these limitations, recent studies have introduced the GGA + U approach, incorporating a Hubbard U parameter to correct self-interaction effects in strongly correlated systems like 3d/4f orbitals.[23,24] For example, Baettig *et al.*[25] found the metallic behavior of Bi_2FeCrO_6 double perovskite using the LDA approach, where the experimentally obtained direct optical bandgap is 1.4 eV.[26] Another investigation by S. Das *et al.*[24] reported that the direct optical bandgap of Gd_2FeCrO_6 is 0.5 eV using the GGA approach, where the experimentally obtained direct optical bandgap is 2.0 eV. As the conventional GGA/LDA techniques understate the bandgap of insulators and semiconductors, the spin-polarized GGA + U approach was used to appropriately represent the effective self-interaction between strongly correlated 4f/3d electrons and address the incorrect description of the bandgap provided by the GGA/LDA approaches.[23,24] According to the Dudarev approach, two free parameters, onsite Coulomb interactions (U) and exchange interactions (J), are combined to produce an effective self-interaction $U_{\text{eff}} = U - J$ between 4f/3d orbitals.[27] Generally, in the GGA + U approach, the values of U_{eff} are chosen in such a way that the computed bandgap aligns well with the experimental outcome.[24,26] For example, Tablero *et al.*[26] found that for $U_{\text{eff}} = 10$ eV, the direct energy bandgap of the Bi_2FeCrO_6 double perovskite matched well with the experimentally obtained direct optical bandgap, and S. Das *et al.*[24] reported that for $U_{\text{eff}} =$ 3 eV, the direct optical bandgap of Gd_2FeCrO_6 matched well with the experimental one.

However, careful selection of the U_{eff} parameter is essential to avoid unintended effects on other material properties when aligning theoretical and experimental bandgap values.[19,23] For example, if U_{eff} is chosen to match the experimental bandgap, one must ensure it does not introduce significant errors in structural parameters or other properties. Previous studies have examined the impact of U_{eff} on the structural and electronic properties of $BiFeO_3$ (BFO). Neaton *et al.*[28] found that using the local spin density approximation (LSDA + U) with $U_{\text{eff}} = 4$ eV improved the accuracy of BFO's crystal parameter, rhombohedral angle, and electronic bandgap. Another study on BFO by Kornev *et al.*[29] reported that parameters within the effective Hamiltonian were highly sensitive to U values, stating that a slight reduction in U from 3.8 to 3.5 eV altered some parameters by around 20%. Therefore, it is crucial to apply an optimal U_{eff} in GGA to closely match the theoretical and experimental bandgap values without significantly affecting the other properties of the material. To our knowledge, no study has yet investigated the effects of the Hubbard U_{eff} parameter on the properties of the GCCO double perovskite. Therefore, in this study, we examined the impact of U_{eff} values on the structural, electronic, and optical properties of our synthesized GCCO nanomaterials through first-principles calculations using both GGA and GGA + U methods. For a reliable theoretical analysis, we used the structural parameters obtained from the experimental one. Finally, considering the theoretically obtained optical bandgap and lattice parameters, the effective Hubbard U potentials for the Co 3d and Cr 3d orbitals of GCCO were determined.

Furthermore, the industrial revolution, alongside the rapid growth in global population, has significantly increased both energy demands and pollution levels.[30,31] This has driven a surge in research aimed at developing renewable energy fuels and advanced purification systems that prioritize efficiency, sustainability, and environmental friendliness. Among the various techniques for energy conversion and pollutant degradation, solar energy utilization has garnered significant attention due to its abundance, low cost, and eco-friendly characteristics.[30–33] Moreover, it is challenging to find potential candidates for photocatalytic and solar energy applications.[31] In this regard, we investigated the relationship between the electronic properties and photocatalytic capabilities, Mott–Schottky (MS) analysis, valence band X-ray photoelectron spectroscopy (XPS), and electrochemical impedance spectroscopy (EIS). These techniques collectively provided a comprehensive understanding of the band structure, carrier dynamics, and redox potentials of GCCO, elucidating its photocatalytic potential for environmental and energy applications.

2. Experimental and computational details

In our previous study,[17] GCCO double-perovskite nanomaterials were prepared using the citrate sol–gel technique. The crystal structure, lattice constants, bond lengths, and bond angles of the prepared GCCO were found through Rietveld-refined X-ray diffraction data. We obtained the absorbance data using UV-visible spectroscopy (UV-2600, Shimadzu) across wavelengths from 200 to 800 nm, and steady-state photoluminescence (PL) spectroscopic measurement was conducted using a PL spectrometer (RF-6000, Shimadzu) at room temperature.

In the present work, we explored the structural parameters and electronic properties—including the band structure, density of states, electron charge density, and Mulliken population analysis—and optical properties, as well as the photocatalytic feasibility of GCCO double perovskite through first-

principles computations and experimental measurements (details in Notes S1 and S2 of the ESI†). We employed both the generalized gradient approximation (GGA) and GGA + U approaches for this computation.

To investigate the as-synthesized GCCO double perovskite theoretically, the first-principles calculation was performed within the plane wave pseudo-potential (PWPP) using the Cambridge-Serial-Total-Energy-Package (CASTEP).[23,34] For this calculation, the lattice constants acquired from the Rietveld analysis of the XRD pattern were employed. Gd ($4f^7\ 5d^1\ 6s^2$), Co ($3d^7\ 4s^2$), Cr ($3d^5\ 4s^1$) and O ($2s^2\ 2p^4$) are considered as outer shell electrons. Prior to further computation, geometry was optimized for optimum cut-off energy and k-points using the Brodyden–Fletcher–Goldfarb–Shanno (BFGS) scheme with an applied energy, maximum force, and maximum stress of 10^{-5} eV per atom, 0.05 eV Å^{-1}, and 0.1 GPa, respectively.[35] The geometry convergence results of GCCO for different energies are illustrated in Fig. 1.

And the geometry convergence results of GCCO for different k-points are illustrated in Fig. 2. In Fig. 1 and 2, the dotted line represents the optimum cut-off energy and k-points found to be 600 eV and $3 \times 2 \times 3$, respectively. Hence, the 600 eV plane wave cut-off energy and $3 \times 2 \times 3$ Monkhorst–Pack k-points mesh were adequate to achieve the optimum structure of the GCCO double perovskite.

Further, the spin-polarized computation was conducted to implement the Hubbard U potential for observing the outcome of the exchange interaction and onsite Coulomb interaction.[27,36] According to previous investigations, the effective value U_{eff} for the 4f orbital was fixed at 6 eV, and U_{eff} values of 3d orbitals were varied from 1 to 6 eV.[23,37]

Moreover, to assess the potential of GCCO as a potential photocatalyst, we performed time resolved photoluminescence spectroscopic measurement using a spectrofluorometer (FS5 spectrofluorometer, Edinburgh Instruments, UK), valence band XPS using a Thermo-Fisher-Scientific X-ray photoelectron spectrometer with an Al K_α (1486.6 eV) X-ray source, and Mott–Schottky analysis utilizing an electrochemical workstation (PGSTAT302N (Autolab), Metrohm, Germany) equipped with a three-electrode system. ESI Note S2† discusses the details of electrochemical measurements.

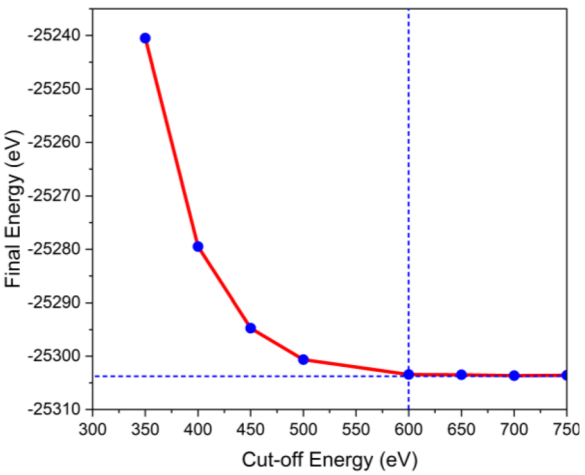

Fig. 1 Optimum cut-off energy for geometry optimization.

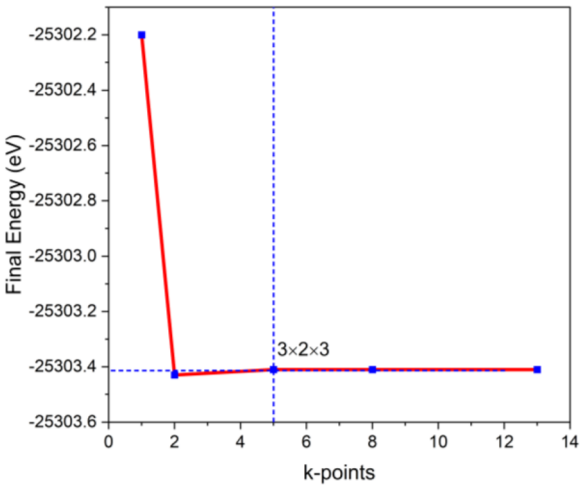

Fig. 2 Optimum k-points for geometry optimization.

3. Results analysis and discussion

3.1 Lattice structure analysis

In our earlier investigation, the lattice structure of GCCO nanomaterials was investigated vigorously through Rietveld refinement of the XRD pattern.[17] This analysis confirmed that GCCO double perovskite exhibits a crystalline monoclinic structure within the $P2_1/n$ space group, with lattice constants of $a = 5.266$ Å, $b = 5.455$ Å, $c = 7.525$ Å, monoclinic angle $\beta = 90.083°$, and a unit cell volume of 216.16 Å^3.

In the current investigation, the structural parameters are investigated using GGA and GGA + U methods. The theoretically obtained lattice constants are illustrated in Table 1. Experimentally obtained lattice parameters are also included together for comparison with theoretically obtained values. It is observed that the theoretically obtained lattice constants align well with experimental findings and increase nominally with an increase of U_{eff} values due to onsite Coulomb repulsion that is consistent with several previous investigations.[19,24]

3.2 Experimentally observed optical features

The optical features of Gd_2CoCrO_6 (GCCO) nanomaterials were systematically investigated to assess their suitability for advanced photocatalytic applications, including environmental cleanup (*e.g.*, wastewater remediation) and energy-related processes such as water splitting, CO_2 reduction, and dye-sensitized solar cells (DSSCs). The study began by evaluating the material's optical bandgap, a critical parameter influencing light absorption and photocatalytic efficiency.[17]

UV-visible absorbance spectroscopy was employed to determine the optical bandgap of GCCO, as shown in Fig. 3(a). The analysis, based on the Tauc relation, revealed a direct bandgap of 2.25 eV.[38] This value is significant, as it places GCCO in the visible light regime of the solar spectrum, where the majority of

Table 1 Theoretically obtained lattice parameters for different Hubbard potentials with experimentally obtained lattice parameters

Lattice parameter	U_{eff} = 0 eV	U_{eff} = 1 eV	U_{eff} = 2 eV	U_{eff} = 3 eV	U_{eff} = 4 eV	U_{eff} = 4.2 eV	U_{eff} = 5 eV	U_{eff} = 6 eV	Experimental value
a (Å)	5.355	5.385	5.382	5.398	5.418	5.425	5.445	5.494	5.266
b (Å)	5.707	5.695	5.696	5.713	5.746	5.753	5.798	5.834	5.455
c (Å)	7.544	7.598	7.659	7.677	7.688	7.692	7.687	7.744	7.525
β (°)	89.846	89.33	89.218	89.209	89.215	89.265	89.40	89.625	90.083
Vol. (Å^3)	230.55	233.01	234.61	236.75	239.34	240.07	242.68	248.21	216.16

solar energy is concentrated, making it a suitable candidate for natural light driven photocatalytic applications.

To further corroborate the optical bandgap, steady-state photoluminescence (PL) spectroscopy was performed, as presented in Fig. 3(b). The PL spectrum exhibited an emission peak at 542 nm, associated with an optical bandgap of 2.28 eV. The close agreement between the UV-visible absorbance and PL measurements confirms that GCCO behaves like a direct bandgap semiconductor, essential for efficient light absorption and electron–hole pair generation. This bandgap of approximately 2.25 eV is particularly advantageous for photocatalytic applications, such as wastewater treatment, where visible light can excite the material to generate charge carriers that initiate redox reactions to degrade organic pollutants. Moreover, the moderate bandgap of GCCO is well-suited for water splitting, as the photogenerated electrons can participate in hydrogen evolution at the conduction band, while the holes in the valence band facilitate oxygen evolution. The energy associated with the bandgap is sufficient to overcome the thermodynamic barriers for water splitting, positioning GCCO as a promising material for sustainable hydrogen production.

In addition to its optical absorption properties, the charge carrier dynamics are pivotal in determining photocatalytic efficiency. To explore this aspect, time-correlated-single-photon-counting (TCSPC) was utilized, providing insights into the excited-state behavior of GCCO. The time-resolved photoluminescence (TRPL) analysis shown in Fig. 3(c) revealed a tri-exponential decay profile, with lifetimes of τ_1 = 0.29 ns, τ_2 = 1.65 ns, and τ_3 = 5.16 ns, yielding a mean carrier lifetime of 2.37 ns. The relatively long carrier lifetime indicates efficient charge separation and reduced electron–hole recombination, which are critical factors for enhancing photocatalytic efficiency.[30] These prolonged carrier lifetimes enable the photogenerated charge carriers to persist long enough to participate in essential chemical reactions. For example, in CO_2 reduction, the long-lived electrons can engage in multi-electron transfer processes necessary for converting CO_2 into hydrocarbons or other valuable products.

3.3 Electronic properties

3.3.1 Band structure calculation. Brand structure is crucial for visualizing the bandgap nature of a material, which is a prerequisite for photocatalytic mechanisms. In this regard, the band structure was computed initially only *via* the GGA approach with U_{eff} = 0 eV. Fig. 4(a) shows the observed band structure, in which the dashed line between conduction bands and valence bands indicates the Fermi energy level.[39] It is noticed that for both the up-spin (red curves) and down-spin (blue curves), the valence bands have crossed the Fermi energy level, which indicates the metallic behavior of GCCO double perovskite. But experimentally, GCCO reveals a direct bandgap semiconducting behavior with a bandgap energy of 2.25 eV. Hence, the band diagrams obtained for U_{eff} = 0 eV were incorrect. Then, to fix the band structure of the GCCO double perovskite, the effective Coulomb interaction was incorporated in the band-structure computation using the GGA + U approach. The band diagrams obtained from the GGA + U approach are shown in Fig. 4(b, c and e) for U_{eff} = 2, 4, and 6 eV and in ESI Fig. S1† for U_{eff} = 1, 3, 4.5, and 5 eV. It is noticed from Fig. 4 that the up-spin configuration is metallic for all values of U_{eff}, and

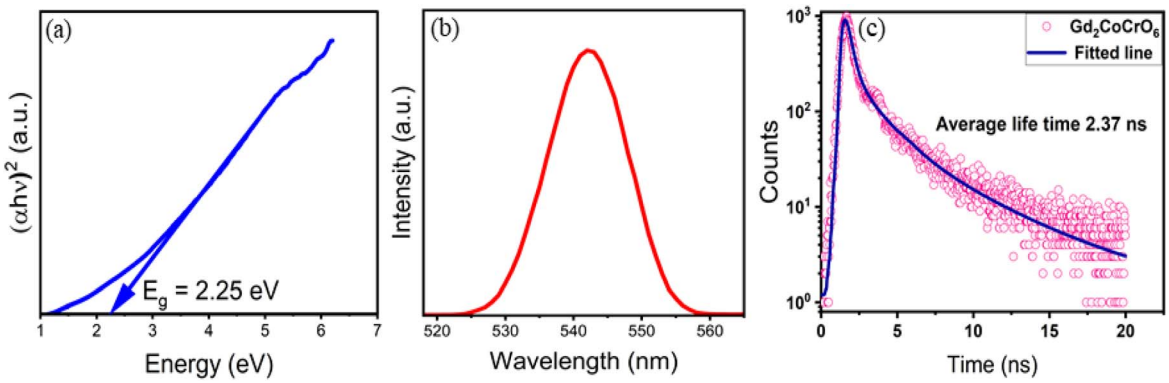

Fig. 3 Experimentally obtained (a) direct optical bandgap, (b) steady-state photoluminescence (PL) spectrum,[17] and (c) time resolved PL spectrum of Gd_2CoCrO_6 nanomaterials.

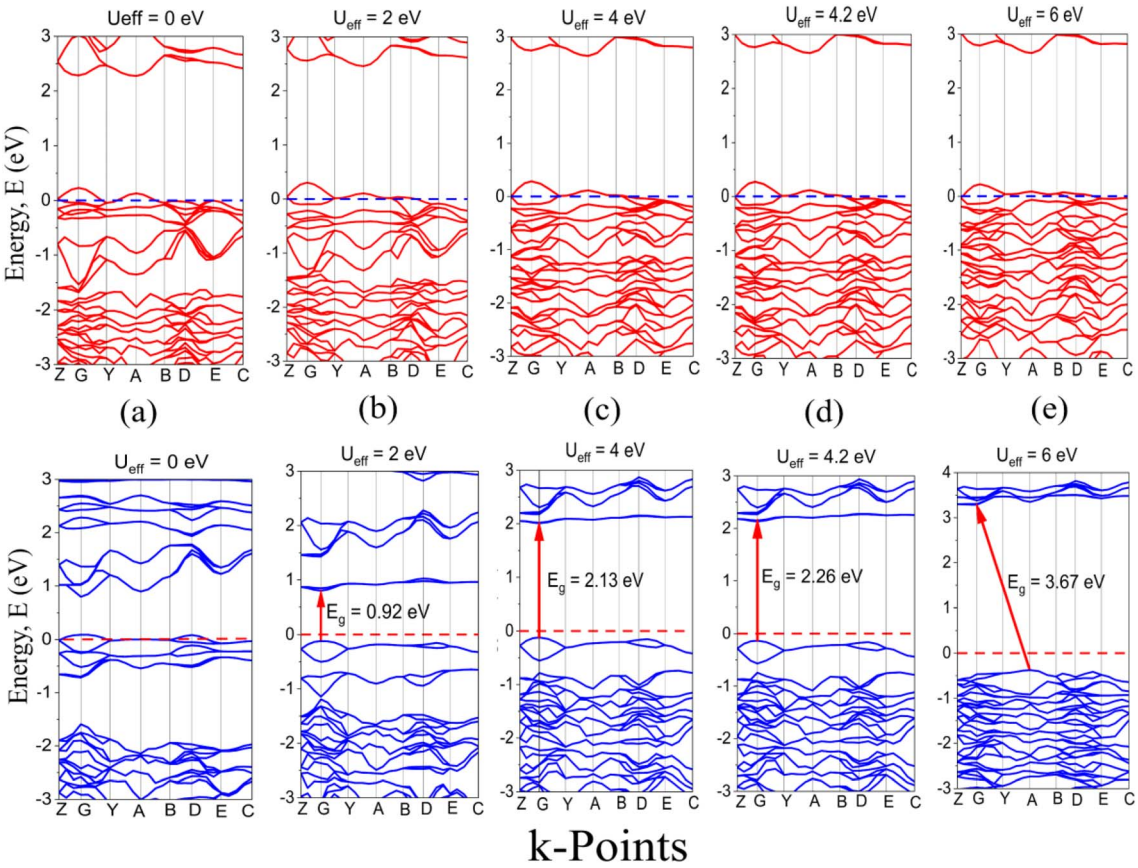

Fig. 4 (a–e) Band diagrams of Gd_2CoCrO_6 for U_{eff} = 0, 2, 4, 4.2, and 6 eV, where red curves represent the up-spin orientation and blue curves represent the down-spin orientation.

bandgap increases with U_{eff} for down-spin orientation, which indicates the half-metallic nature of the GCCO double perovskite.[23,37]

Moreover, the bandgap found for U_{eff} = 4 eV was 2.13 eV, which was slightly lower than the experimentally obtained value of 2.25 eV. Then, for exact U correction, the calculation was conducted again with U_{eff} = 4.5 and 4.2 eV. After that, the bandgap was determined to be 2.26 eV for Hubbard correction U_{eff} = 4.2 eV, shown in Fig. 4(d), which closely matched the experimentally obtained value. It is also noticeable that the conduction-band-minimum (CBM) and valence-band-maximum (VBM) are in the same symmetric line, which indicates the direct bandgap nature of GCCO that is crucial for photocatalytic efficiency. Further, it is seen from Fig. 4 that the bandgaps are found within the range of the semiconductor for the U_{eff} values up to 5 eV. For U_{eff} = 6 eV, the bandgap is found to be indirect and in the range of the insulator, which provides the limitation on employing larger U_{eff} values greater than 5 eV in the first-principles calculation of the GCCO double-perovskite.[19]

3.3.2 Density of states. To check whether all distinct orbitals are attributed to the band structure, the total and partial densities of states (TDOS and PDOS) for Gd(4f), Co(3d), Cr(3d), and O(2p) orbitals were computed using both the GGA and GGA + U methods.[24] A higher density of states (DOS) represents higher available states for occupation, and a lower DOS represents lower available states for occupation. A zero DOS represents no available state for occupation. Fig. 5 shows the TDOS and PDOS for U_{eff} = 0, 2, 4, 4.2, and 6 eV, and ESI Fig. S2† shows the TDOS and PDOS for U_{eff} = 1, 3, 4.5, and 5 eV both for down-spin and up-spin orientations. In Fig. 5, the density of states above the Fermi level ($E - E_F > 0$ eV) represents the conduction band, and the DOS below the Fermi level ($E - E_F < 0$ eV) represents the valence band. It is seen from Fig. 5(a) that, for up-spin orientation, the conduction band near 2.6 eV is formed by the hybridization of Cr(3d) and O(2p) orbitals with a major contribution from Cr(3d) orbitals and a small contribution from O(2p) orbitals; the band around 6 eV is due to the contribution from other orbital states of the Gd_2CoCrO_6 double perovskite; the valence band near −0.2 eV is formed by the major contribution of Cr(3d) orbitals and minor contribution of O(2p) orbitals; the band around −2.7 eV is due to O(2p) orbitals and Co(3d) orbitals; and the band at −5 eV is formed by the major contribution of Gd(4f) orbitals and minor contribution of Co(3d) and O(2p) orbitals.

Now, for the down-spin configuration, the conduction bands near 1.3, 3, and 7 eV are formed by the contribution of Co(3d), Gd(4f), and other orbitals, respectively; the valence band near −0.3 eV is composed of Co(3d) and O(2p) orbitals; and the band around −4 eV is due to O(2p) orbitals. It is also noticeable that

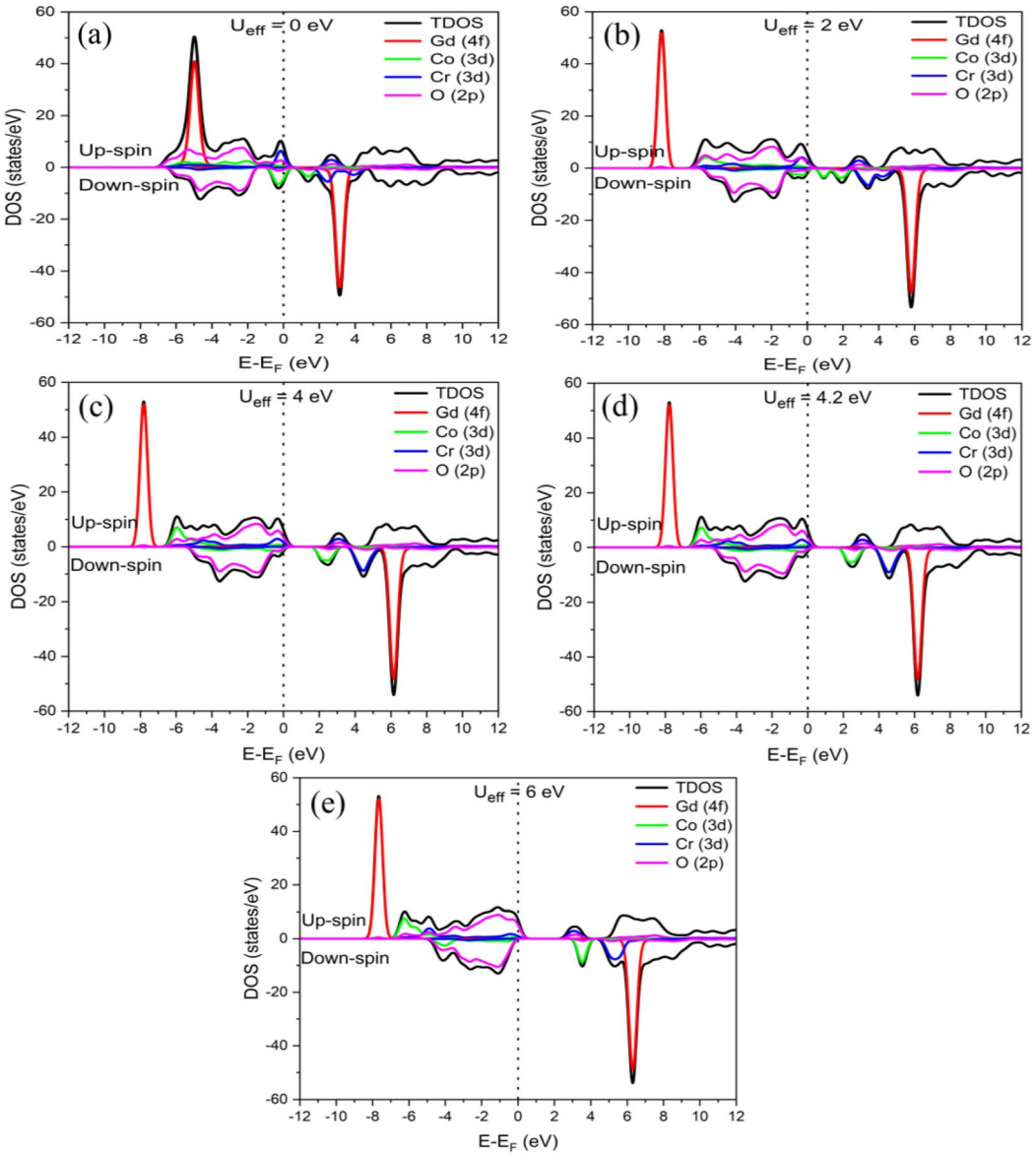

Fig. 5 Total and partial densities of states (TDOS and PDOS) of Gd(4f) orbitals, Co(3d) orbitals, Cr(3d) orbitals, and O(2p) orbitals for U_{eff} values of (a) 0 eV, (b) 2 eV, (c) 4 eV, (d) 4.2 eV, and (e) 6 eV.

the density of states shifted towards larger energy values with an increase of U_{eff} values due to the onset of Coulomb repulsion which also indicates the increment of bandgap with an increase of U values.[19] Moreover, the computed spin density for the effective Hubbard correction $U_{eff} = 4.2$ eV is found to be $13\mu_B$ per formula unit, an integer value that unequivocally supports the half-metallic character of GCCO in its ground state. This finding aligns well with theoretical expectations for half-metallic materials, as discussed by Pickett and Moodera.[40] The integer magnetic moment arises due to the complete spin polarization of the electronic states, which is a hallmark of half-metallic behavior.

3.3.3 Distribution of electron charge density. Further, to visualize the bonding nature of the GCCO double perovskite, the electron charge density was determined for the (110) plane using both GGA ($U_{eff} = 0$ eV) and GGA + U ($U_{eff} = 2$, 4, and 6 eV) approaches and the outcomes are illustrated in Fig. 6. It is noteworthy that the covalent bond is formed when electron clouds of two atoms overlap, and electrons become concentrated in the overlapping region.[41]

It is seen from Fig. 6 that for all values of U_{eff}, the overlapping region between Co/Cr and O atoms is larger than the overlapping region of Gd and O atoms. This outcome indicates the formation of covalent bonds and reveals that the Co/Cr–O covalent bond is stronger than the Gd–O covalent bond. It is also observed from the DOS curve in Fig. 5 that the charge sharing among the Co/Cr and O bonds is due to the hybridization of Co/Cr(3d) orbitals and O(2p) orbitals, and the charge sharing among the Gd and O bonds is due to the hybridization of Gd(4f) orbitals and O(2p) orbitals. There is another observation in Fig. 6 that there is no overlapping region between two of the four Gd atoms and the O atom, which indicates the

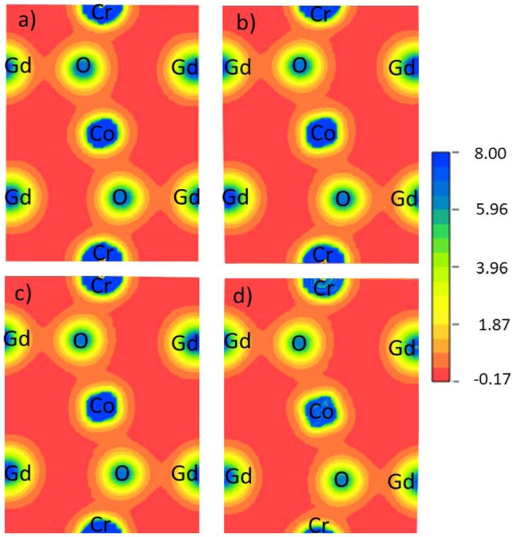

Fig. 6 Electron charge density distribution for U_{eff}: (a) 0 eV, (b) 2 eV, (c) 4 eV, and (d) 6 eV.

presence of ionic bonding between the Gd and O atoms.[23,42] Moreover, the presence of both ionic and covalent bonding further increases the photocatalytic excellency by lowering the recombination rate of electron–hole pairs and increasing the charge carriers' mobility.

3.3.4 Mulliken population analysis. Mulliken population analysis was conducted to gain deeper insight into the effective atomic charge, bond population, and bond length of the GCCO double perovskite using both GGA and GGA + U techniques.[43,44] The effective Mulliken charge Q (μ) of a certain atom μ can be expressed as,[24,43]

$$Q(\mu) = \sum_k \omega_k \sum \sum_{\alpha}^{\text{on }\mu} \sum_{\beta} P_{\alpha\beta}(k) S_{\alpha\beta}(k) \quad (1)$$

where $P_{\alpha\beta}$ and $S_{\alpha\beta}$ denote the density-matrix and overlap-matrix, respectively. Again, the bond population P (μν) between atoms μ and ν can be computed using the following formula,[24,43]

$$P(\mu\nu) = \sum_k \omega_k \sum \sum_{\alpha}^{\text{on }\mu} \sum_{\beta}^{\text{on }\nu} 2P_{\alpha\beta}(k) S_{\alpha\beta}(k) \quad (2)$$

The results found from the Mulliken population analysis are presented in Table 2. It is noticed from Table 2 that the observed effective Mulliken charges of Gd, Co, Cr, and O are noticeably smaller compared to their formal charges of +3, +2, +3, and −2, respectively, for all values of U_{eff}, which reveals the existence of mixed bonding (covalent and ionic).[44] The existence of mixed bonding is also shown by the charge density distribution in Fig. 6. Moreover, the lower effective charge indicates higher covalency hence the covalent bond is prominent in the GCCO double perovskite.[23,44] Further, an increment can be noticed with an increase in U_{eff} values which is due to a decrease in covalency as a result of onsite Coulomb repulsion.

Table 2 further represents the bond population and bond length present in the GCCO double perovskite. It is observed from bond population calculation that the Cr–O and Co–O bond populations are higher compared to the bond population of the Gd–O bond. It is noteworthy that the higher degree of bond population is related to a higher degree of covalency and *vice versa*.[45] This suggests that the Cr–O and Co–O bonds have a greater level of covalency than the Gd–O bond, which is also consistent with electron charge density distribution, as illustrated in Fig. 6. It is further noticeable that the O–O bond population is negative, which indicates no bonding between two oxygen atoms.[37,46]

Finally, Table 2 presents the bond lengths, and it is seen that the Cr–O and Co–O bond lengths are lower than the bond length of the Gd–O bond as a result of a larger degree of covalency and higher bond population of Cr–O and Co–O bonds. An

Table 2 Effective Mulliken charges, bonds population, and bonds lengths of the GCCO double perovskite

	GGA	GGA + U				
Atoms	U_{eff} = 0 eV	U_{eff} = 1 eV	U_{eff} = 2 eV	U_{eff} = 3 eV	U_{eff} = 4 eV	U_{eff} = 5 eV	U_{eff} = 6 eV
Effective Mulliken charges (*e*)							
Gd	1.48	1.50	1.51	1.51	1.51	1.52	1.52
Co	0.65	0.66	0.67	0.68	0.68	0.69	0.69
Cr	0.55	0.56	0.57	0.58	0.59	0.60	0.63
O	−0.69	−0.70	−0.71	−0.71	−0.72	−0.72	−0.73
Bonds	**Bonds population**						
Gd–O	0.149	0.153	0.154	0.156	0.159	0.164	0.173
Co–O	0.280	0.277	0.277	0.273	0.273	0.270	0.260
Cr–O	0.367	0.367	0.360	0.353	0.343	0.330	0.323
O–O	−0.031	−0.034	−0.032	−0.031	−0.030	−0.03	−0.028
Bonds	**Bonds length (Å)**						
Gd–O	2.464	2.475	2.480	2.484	2.489	2.494	2.506
Co–O	2.052	2.059	2.064	2.070	2.077	2.085	2.115
Cr–O	1.976	1.982	1.991	1.999	2.013	2.032	2.047

increment of bond length with an increment of U_{eff} was also observed because of onsite Coulomb repulsion.

3.4 Theoretically obtained optical properties

The optical properties and absorption coefficients of the GCCO double-perovskite were determined utilizing both GGA and GGA + U approaches adopting the following formula,[47]

$$\alpha(\omega) = \sqrt{2\omega\left(\sqrt{\varepsilon_1^2(\omega) + \varepsilon_2^2(\omega)} - \varepsilon_1(\omega)\right)} \quad (3)$$

where $\alpha(\omega)$ is the absorption coefficient, $\varepsilon_2(\omega)$ and $\varepsilon_1(\omega)$ are the imaginary and real parts of the complex dielectric function and ω is photon frequency.

The computed absorption coefficients as a function of the wavelength of the GCCO double perovskite for different U_{eff} values are illustrated in Fig. 7(a). From Fig. 7(a), two absorption peaks are clearly observed at the wavelengths of 115 nm and around 300 nm. Both are within the UV region, which indicates that the GCCO double perovskite is a strong UV light absorber.

It is also noteworthy that the absorption peak at 150 nm underwent a redshift with an increase of U_{eff} values, and the absorption peak around 300 nm underwent a blue shift with an increase of U_{eff} values as a result of the increment of bandgap as shown in Fig. 4.[24] Notably, the spectrum derived from the experiment, as displayed in ESI Fig. S3,† contains two additional visible spectrum bands in addition to the two bands observed theoretically in the UV range. This might be because the experiment was performed at room temperature, whereas the DFT computations were performed at 0 K.[48,49] Moreover, the bandgap calculated for U_{eff} = 4.2 eV using the theoretical absorption data is 2.25 eV, as demonstrated in Fig. 7(b), which is also consistent with the experimentally obtained bandgap of the GCCO double perovskite.

3.5 Comparison of theoretical and experimental optical bandgaps

Additionally, utilizing the Tauc relation and the theoretically obtained absorption coefficients, we estimated the optical bandgap values of the GCCO nanomaterials.[38] The change in the theoretically computed direct bandgap values as a function of U_{eff} is depicted in Fig. 8. Notably, the GGA approach yielded a direct bandgap value of 1.77 eV (U_{eff} = 0 eV), considerably lower than the experimental value of 2.25 eV. The direct optical bandgap values of the GCCO double perovskite also show a nearly linear increase with an increase in U_{eff} from 1 to 4.2 eV. Moreover, an unexpected reduction can be seen for an additional rise in U_{eff} to 6 eV. Interestingly, the direct optical bandgap (2.25 eV) predicted for U_{eff} = 4.2 eV coincides with the experimentally observed direct optical bandgap found from the Tauc relation (2.25 eV), which is denoted by a blue circle in Fig. 8.

In the end, our findings reveal that a U_{eff} value of 4.2 eV captures the essence of GCCO's structural, electronic, and optical characteristics with remarkable precision, aligning seamlessly with experimental observations. This value finely tunes the localization of the 3d orbitals of Co and Cr, striking a perfect balance without overestimating or underestimating the bandgap.

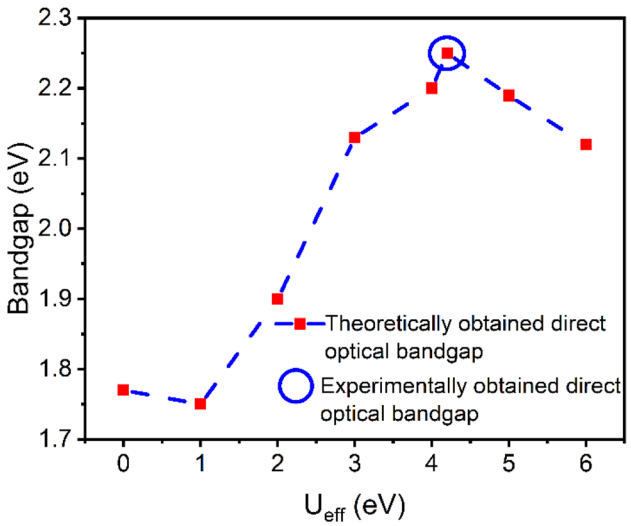

Fig. 8 Theoretically obtained direct optical bandgap as a function of U_{eff}. The experimentally determined optical bandgap value is depicted by the blue circle.

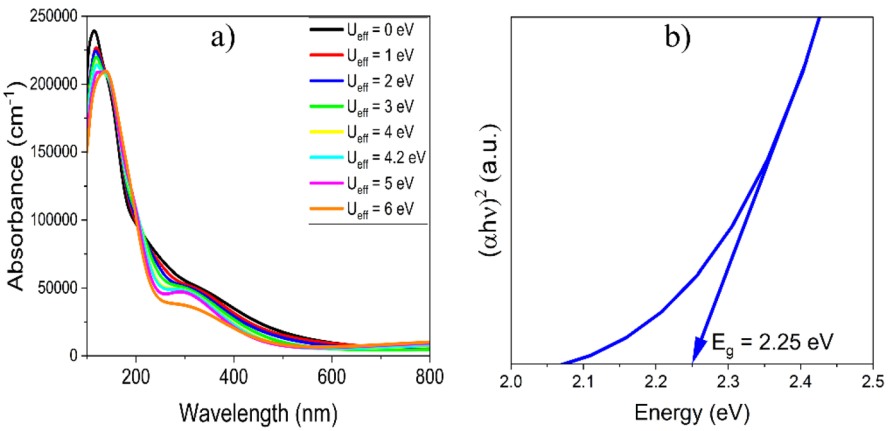

Fig. 7 (a) Theoretically obtained absorbance for U_{eff} = 0 to 6 eV and (b) bandgap obtained from the Tauc plot for U_{eff} = 4.2 eV.

Moreover, the exceptional accuracy in bandgap prediction highlights the minimal influence of self-interaction errors from other GCCO orbitals.[22,50] Therefore, we recommend $U_{eff} = 4.2$ eV as the optimal choice for GGA + U calculations, providing a reliable and accurate framework for understanding the atomic-level properties of GCCO.

Finally, we have conducted a comparative study between lattice parameters and the electronic bandgap of GCCO with previously investigated similar double perovskites, as shown in Table 3. It is observed from Table 3 that the conventional GGA/LDA approaches underestimate the bandgap due to self-interaction error of strongly correlated 4f/3d orbitals. It is also seen from Table 3 that the implementation of a precise effective Hubbard U potential appropriately represents the effective self-interaction between strongly correlated 4f/3d electrons and addresses the incorrect description of bandgap provided by the GGA/LDA approaches. Table 3 also represents the comparison between optimized lattice parameters obtained from GGA/LDA + U approaches and experimentally measured lattice parameters and the deviation is minimal.

3.6 Mott–Schottky and valence band XPS analysis

The electronic structure of Gd_2CoCrO_6 (GCCO) nanomaterials is crucial for their photocatalytic performance. To investigate the relationship between the electronic properties and photocatalytic capabilities, Mott–Schottky (MS) analysis, valence band XPS, and electrochemical impedance spectroscopy (EIS) were utilized.[53–57] These techniques collectively provided a comprehensive understanding of the band structure, carrier dynamics, and redox potentials of GCCO, elucidating its photocatalytic potential for environmental and energy applications.

Mott–Schottky analysis, shown in Fig. 9(a), was conducted to determine the semiconductor type and flat-band potential (E_{fb}) of GCCO. The MS plot exhibited a quasi-linear behavior with a negative x-intercept, confirming that GCCO is an n-type semiconductor.[54–57] This is significant because n-type materials have an excess of electrons, making them suitable for reduction reactions driven by photogenerated electrons.[30,58,59] The flat-band potential was measured to be −0.28 V *versus* Ag/AgCl, reflecting the energetic conduction band edge position. Using the standard relation between the flat-band potential and conduction-band-minimum (E_{CBM}), the conduction band potential of GCCO was calculated to be −2.18 V *vs.* Ag/AgCl, or −1.983 V on the normal hydrogen electrode (NHE) scale.[30,59] This highly negative conduction band potential is crucial for photocatalytic applications, as it indicates that the photogenerated electrons in GCCO have sufficient energy to drive reduction reactions, such as hydrogen evolution (H^+ to H_2) and oxygen reduction (O_2 to O^{2-}).[58]

The valence band position (E_{VBM}) was determined from valence band XPS measurements. The valence band edge was found to be 0.253 V *versus* NHE, which aligns well with theoretical calculations based on the relation $E_{VBM} = E_{CBM} + E_g$, where E_g is the optical bandgap.[30,54–57,60] The valence band edge position was determined using the conduction band minimum from the Mott–Schottky analysis and the bandgap from the Tauc plot, as shown in Fig. 9(c). This positive potential of the valence band promotes the photogenerated holes in GCCO to oxidize hydroxyl ions (OH^-) to hydroxyl radicals ($OH^\bullet$), which are highly reactive species essential for degrading organic pollutants in wastewater.[30] The ability of GCCO to participate in both oxidation and reduction reactions highlights its versatility in photocatalytic applications.

Further insights into the photocatalytic behavior of GCCO were provided by electrochemical impedance spectroscopy (EIS). The Nyquist plot, shown in Fig. 9(d), revealed a small arc radius for GCCO, indicative of low charge transfer resistance. This feature is crucial for efficient charge separation and minimal electron–hole recombination, a common challenge in photocatalysis. Efficient charge separation ensures that both the conduction-band electrons and valence-band holes remain available to drive their respective redox reactions, thus enhancing overall photocatalytic efficiency.

The alignment of GCCO's band positions with the redox potentials for key photocatalytic reactions supports its

Table 3 A comparative analysis of lattice parameters, and electronic bandgap of Gd_2CoCrO_6 and similar previously investigated double perovskites

Materials	Lattice parameters (optimized) (Å)	Lattice parameters (exp.) (Å)	Bandgap (GGA/LDA) (eV)	Bandgap (GGA/LDA + U) (eV)	Bandgap (exp.) (eV)	Effective Hubbard U parameter (eV)	Ref.
Gd_2CoCrO_6	$a = 5.425$ $b = 5.753$ $c = 7.692$	$a = 5.266$ $b = 5.455$ $c = 7.525$	Metallic	2.25	2.25	$U_{Co} = 4.2$ $U_{Cr} = 4.2$	Present work
Gd_2FeCrO_6	$a = 5.457$ $b = 5.689$ $c = 7.808$	$a = 5.359$ $b = 5.590$ $c = 7.675$	0.50	1.99	2.0	$U_{Fe} = 3$ $U_{Cr} = 3$	24
Sr_2ZnMoO_6	$a = b = 5.655$ $c = 8.006$	$a = b = 5.583$ $c = 7.979$	1.992	2.89	2.7	$U_{Zn} = 10$ $U_O = 7$	51
Bi_2FeCrO_6	$a = b = c = 5.55$	$a = b = c = 5.47$	Metallic	1.41	1.4	$U_{Fe} = 10$ $U_{Cr} = 10$	25 and 26
Nd_2NiMnO_6	—	$a = 5.415$ $b = 5.484$ $c = 7.674$	—	1.441	1.5	$U_{Ni} = 4$ $U_{Mn} = 4$	52

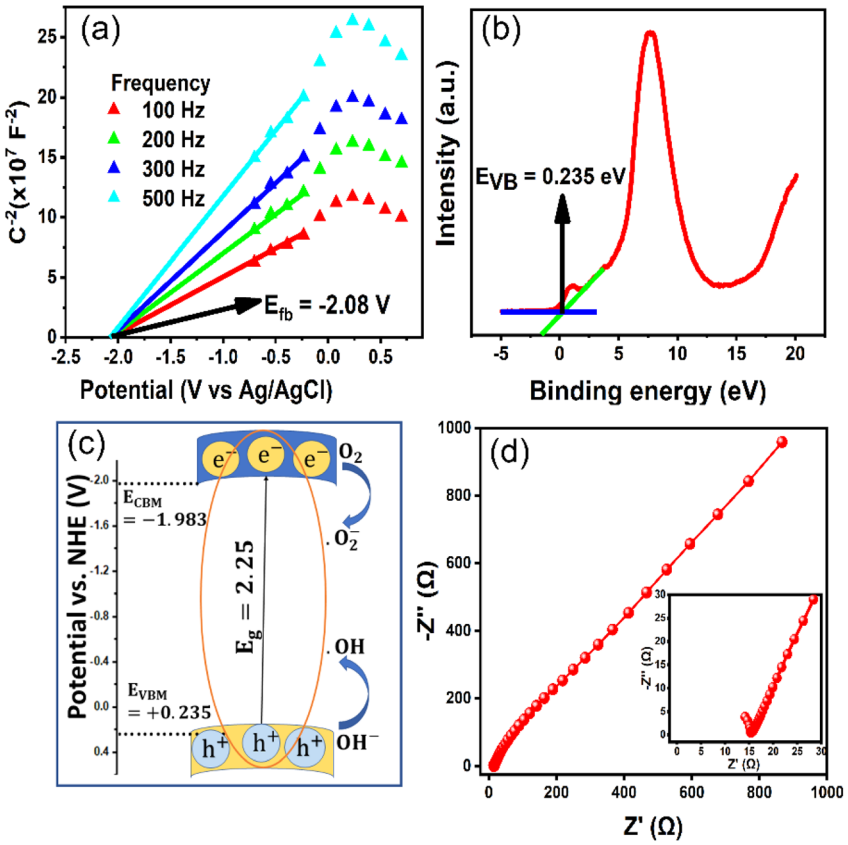

Fig. 9 (a) Mott–Schottky curve at different frequencies, (b) valence band XPS spectrum, (c) band edge position, and (d) Nyquist plot of GCCO nanomaterials. The onset of (d) shows the high-frequency region of the Nyquist plot.

suitability for a wide range of applications. The highly negative conduction band position is advantageous for proton reduction to hydrogen and oxygen reduction to superoxide ions, while the valence band enables the oxidation of hydroxyl ions and organic contaminants.[30,57] This dual capability underscores the potential of GCCO for application in water splitting, CO_2 reduction, and environmental remediation.

4. Conclusions

This study presents a thorough theoretical and experimental investigation of Gd_2CoCrO_6 (GCCO) double perovskite, establishing its significant potential as a high-performance photocatalyst. Theoretical analyses using GGA + *U* reveal that GCCO possesses a direct bandgap in the visible spectrum and a half-metallic electronic structure, with spin-dependent properties that optimize charge carrier dynamics. The incorporation of Hubbard *U* correction effectively localizes the Co 3d and Cr 3d orbitals, enhancing the accuracy of electronic structure predictions while maintaining the material's structural parameters. Detailed charge density distribution and Mulliken population analyses confirm a mixed ionic-covalent bonding nature, which contributes to the material's stability and efficient charge mobility. Experimentally, UV-visible and photoluminescence spectroscopy confirm a direct bandgap suitable for visible light absorption, with excellent agreement with theoretical predictions. Time-resolved photoluminescence reveals extended charge carrier lifetimes, reducing recombination rates, and enabling efficient charge separation. Electrochemical impedance spectroscopy further validates its low charge transfer resistance, critical for sustaining high photocatalytic activity. Mott–Schottky and XPS analyses confirm GCCO as an n-type semiconductor with conduction and valence band edge positions ideally suited for photocatalytic water splitting, pollutant degradation, and CO_2 reduction. The material's highly negative conduction band minimum facilitates proton reduction to hydrogen, while the valence band position supports oxidative processes, ensuring its dual functionality for both reduction and oxidation reactions. The results position GCCO as an advanced photocatalyst capable of leveraging visible light for solar-driven processes such as hydrogen evolution, oxygen evolution, and the degradation of organic pollutants, addressing critical energy and environmental challenges. This study also highlights GCCO's stability, versatility, and scalability for practical applications. Future work should focus on compositional engineering, such as doping or defect modulation, to enhance photocatalytic efficiency further. The implications of this research extend beyond the characterization of a single material. It provides a robust framework for systematically investigating other double perovskites with complex electronic interactions, thereby paving the way for designing efficient materials for energy and

environmental applications. Future studies will explore doping strategies to optimize the bandgap and improve charge carrier dynamics, enhancing the applicability of GCCO in real-world photocatalytic systems.

Data availability

The data supporting this article have been included as part of the ESI.†

Conflicts of interest

There are no conflicts to declare.

Acknowledgements

The computational facilities provided by the GPU workstation, Department of Physics, University of Dhaka and Nanotechnology Research Laboratory, Bangladesh University of Engineering and Technology (BUET) are gratefully acknowledged.

Notes and references

1 A. S. Bhalla, R. Guo and R. Roy, *Mater. Res. Innovations*, 2000, **4**, 3–26.
2 M. A. Basith, O. Kurni, M. S. Alam, B. L. Sinha and B. Ahmmad, *J. Appl. Phys.*, 2014, **115**, 024102.
3 S. Vasala and M. Karppinen, *Prog. Solid State Chem.*, 2015, **43**, 1–36.
4 M. Shang, C. Zhang, T. Zhang, L. Yuan, L. Ge, H. Yuan and S. Feng, *Appl. Phys. Lett.*, 2013, **102**, 062903.
5 T. Saha-Dasgupta, *Mater. Res. Express*, 2020, **7**, 014003.
6 M. D. I. Bhuyan, S. Das and M. A. Basith, *J. Alloys Compd.*, 2021, **878**, 160389.
7 K. I. Kobayashi, T. Kimura, H. Sawada, K. Terakura and Y. Tokura, *Nature*, 1998, **395**, 677–680.
8 N. Das, S. Singh, A. G. Joshi, M. Thirumal, V. R. Reddy, L. C. Gupta and A. K. Ganguli, *Inorg. Chem.*, 2017, **56**, 12712–12718.
9 R. J. Cava, B. Batlogg, J. J. Krajewski, R. Farrow, L. W. Rupp, A. E. White, K. Short, W. F. Peck and T. Kometani, *Nature*, 1988, **332**, 814–816.
10 H. Tanaka and M. Misono, *Curr. Opin. Solid State Mater. Sci.*, 2001, **5**, 381–387.
11 M. A. Basith, S. Manjura Hoque, M. Shahparan, M. A. Hakim and M. Huq, *Phys. B Condens. Matter*, 2007, **395**, 126–129.
12 S. Halder, M. S. Sheikh, R. Maity, B. Ghosh and T. P. Sinha, *Ceram. Int.*, 2019, **45**, 15496–15504.
13 P. Shirazi, M. Rahbar, M. Behpour and M. Ashrafi, *New J. Chem.*, 2020, **44**, 231–238.
14 R. Mohassel, M. Amiri, A. K. Abbas, A. Sobhani, M. Ashrafi, H. Moayedi and M. Salavati-Niasari, *J. Mater. Res. Technol.*, 2020, **9**, 1720–1733.
15 C. Lin, Y. Zhao, Y. Liu, W. Zhang, C. Shao and Z. Yang, *J. Mater. Res. Technol.*, 2021, **11**, 1645–1653.
16 B. Gray, H. N. Lee, J. Liu, J. Chakhalian and J. W. Freeland, *Appl. Phys. Lett.*, 2010, **97**, 013105.
17 M. J. Hosen, M. A. Basith and I. M. Syed, *RSC Adv.*, 2023, **13**, 17545–17555.
18 R. Zhang, J. Zhao, Y. Yang, Z. Lu and W. Shi, *Comput. Condens. Matter*, 2016, **6**, 5–17.
19 J. K. Shenton, D. R. Bowler and W. L. Cheah, *J. Phys.: Condens. Matter*, 2017, **29**, 445501.
20 B. Himmetoglu, A. Floris, S. de Gironcoli and M. Cococcioni, *Int. J. Quantum Chem.*, 2014, **114**, 14–49.
21 K. Terakura, T. Oguchi, A. R. Williams and J. Kübler, *Phys. Rev. B: Condens. Matter Mater. Phys.*, 1984, **30**, 4734.
22 J. J. Brown and A. J. Page, *J. Chem. Phys.*, 2020, **153**, 224116.
23 R. Rozilah, M. K. Yaakob, Z. Mohamed and A. K. Yahya, *Mater. Res. Express*, 2017, **4**, 066103.
24 S. Das, M. D. I. Bhuyan and M. A. Basith, *J. Mater. Res. Technol.*, 2021, **13**, 2408–2418.
25 P. Baettig, C. Ederer and N. A. Spaldin, *Phys. Rev. B: Condens. Matter Mater. Phys.*, 2005, **72**, 214105.
26 C. Tablero, *Sol. Energy*, 2016, **137**, 173–178.
27 S. L. Dudarev, G. A. Botton, S. Y. Savrasov, C. J. Humphreys and A. P. Sutton, *Phys. Rev. B:Condens. Matter Mater. Phys.*, 1998, **57**, 1505.
28 J. B. Neaton, C. Ederer, U. V. Waghmare, N. A. Spaldin and K. M. Rabe, *Phys. Rev. B: Condens. Matter Mater. Phys.*, 2004, **71**, 014113.
29 I. A. Kornev, S. Lisenkov, R. Haumont, B. Dkhil and L. Bellaiche, *Phys. Rev. Lett.*, 2007, **99**, 227602.
30 M. Tarek, F. Yasmeen and M. A. Basith, *J. Mater. Chem. A*, 2024, **12**, 25475.
31 F. Sharmin and M. A. Basith, *J. Alloys Compd.*, 2022, **901**, 163604.
32 D. Champier, *Energy Convers. Manag.*, 2017, **140**, 167–181.
33 N. Sezer and M. Koç, *Nano Energy*, 2021, **80**, 105567.
34 M. D. Segall, P. J. D. Lindan, M. J. Probert, C. J. Pickard, P. J. Hasnip, S. J. Clark and M. C. Payne, *J. Phys. Condens. Matter*, 2002, **14**, 2717–2744.
35 T. H. Fischer and J. Almlöf, *J. Phys. Chem.*, 1992, **96**, 9768–9774.
36 J. T. Zhang, X. M. Lu, J. Zhou, J. Su, K. L. Min, F. Z. Huang and J. S. Zhu, *Phys. Rev. B: Condens. Matter Mater. Phys.*, 2010, **82**, 224413.
37 M. Chakraborty, P. Pal and B. R. Sekhar, *Solid State Commun.*, 2008, **145**, 197–200.
38 J. Tauc, R. Grigorovici and A. Vancu, *Phys. Status Solidi B*, 1966, **15**, 627–637.
39 Y. S. Hou, H. J. Xiang and X. G. Gong, *Phys. Rev. B: Condens. Matter Mater. Phys.*, 2014, **89**, 064415.
40 W. E. Pickett and J. S. Moodera, *Phys. Today*, 2001, **54**, 39–44.
41 J. C. Phillips, *Phys. Rev.*, 1968, **166**, 832–838.
42 D. P. Craig, A. Maccoll, R. S. Nyholm, L. E. Orgel and L. E. Sutton, *J. Chem. Soc.*, 1954, 332.
43 R. S. Mulliken, *J. Chem. Phys.*, 1955, **23**, 1833–1840.
44 M. D. Segall, R. Shah, C. J. Pickard and M. C. Payne, *Phys. Rev. B: Condens. Matter Mater. Phys.*, 1996, **54**, 16317–16320.
45 W. Y. Ching and Y. N. Xu, *Phys. Rev. B: Condens. Matter Mater. Phys.*, 1999, **59**, 12815.
46 M. K. Yaakob, M. F. M. Taib, L. Lu, O. H. Hassan and M. Z. A. Yahya, *Mater. Res. Express*, 2015, **2**, 116101.

47 M. Tamer, *AIP Adv.*, 2016, **6**, 065115.
48 K. Harun, N. A. Salleh, B. Deghfel, M. K. Yaakob and A. A. Mohamad, *Results Phys.*, 2020, **16**, 102829.
49 L. Honglin, L. Yingbo, L. Jinzhu and Y. Ke, *J. Alloys Compd.*, 2014, **617**, 102–107.
50 J. P. Perdew, *Int. J. Quantum Chem.*, 1986, **30**, 451.
51 S. Zhao, C. Lan, J. Ma, S. S. Pandey, S. Hayase and T. Ma, *Solid State Commun.*, 2015, **213–214**, 19–23.
52 S. Abass, F. A. Najar, R. Samad and K. Sultan, *Solid State Commun.*, 2021, **338**, 114463.
53 M. A. Islam, M. Tarek, M. A. Adib and M. A. Basith, *J. Phys. Appl. Phys.*, 2024, **57**, 215302.
54 F. Yasmeen, M. Tarek and M. A. Basith, *ACS Appl. Mater. Interfaces*, 2024, **16**, 47535–47550.
55 M. Tarek and M. A. Basith, *J. Mater. Chem. C*, 2023, **11**, 16605–16622.
56 M. Tarek, F. Yasmeen and M. A. Basith, *J. Mater. Chem. A*, 2025, **13**, 499–516.
57 M. M. Rahman, F. Yasmeen, M. Tarek and M. A. Basith, *J. Alloys Compd.*, 2025, **1010**, 177295.
58 E. Gao, W. Wang, M. Shang and J. Xu, *Phys. Chem. Chem. Phys.*, 2011, **13**, 2887–2893.
59 C. Wan, L. Zhou, L. Sun, L. Xu, D. Cheng, F. Chen, X. Zhan and Y. Yang, *Chem. Eng. J.*, 2020, **396**, 125229.
60 M. M. Islam, M. A. Islam, R. Hossain, M. J. Hosen and M. D. I. Bhuyan, *Phys. B Condens. Matter*, 2024, **692**, 416368.